# Object-Based Classification of PolSAR Images Based on Spatial and Semantic Features

Bin Zou, *Senior Member, IEEE*, Xiaofang Xu, and Lamei Zhang, *Senior Member, IEEE*

***Abstract*—High-resolution polarimatric synthetic aperture radar (PolSAR) images can provide more detail information on land-cover types and increase the image complexity at the same time. Traditionally, pixel-based image classification that takes image pixel as a processing unit cannot make full use of various features contained in high-resolution remote sensing images, and thus may not obtain satisfactory results. Hence, object-based image classification (OBIC) methods using image objects as processing units have been introduced into the PolSAR image classification. However, current researches on OBIC methods for PolSAR images usually could not take advantage of multiscale information of image objects, leading to some results that are not as satisfactory as expected. In this article, a multilevel image description consisting of proposed pixel-level spatial and object-level semantic features is developed for OBIC of PolSAR images. At the image pixel level, based on th combination of polarimetric and morphological image descriptions, polarimetric morphological profiles are developed to describe pixel-level spatial features. At the image object level, based on the construction of object adjacent graph, an object-level semantic indicator is proposed, which takes into account the contextual neighborhood of image objects. Finally, the proposed pixel-level spatial and object-level semantic features are integrated and incorporated in an OBIC scheme for the PolSAR image classification. Two fully polarized datasets acquired by ESAR and uninhabited airborne vehicle synthetic aperture radar (UAVSAR), respectively, are adopted to evaluate the effectiveness of the proposed method. The experimental results validate that the comprehensive utilization of both pixel-level and object-level features can effectively improve the OBIC accuracy of PolSAR images.**

***Index Terms*—High-resolution polarimatric SAR (PolSAR) image, object-based image classification (OBIC), morphological profiles, semantic, segmentation.**

## I. Introduction

BECAUSE of the all-time and all-weather working characteristics of synthetic aperture radar (SAR) system, SAR images have been widely utilized in applications such as land cover monitoring, damage assessment, agriculture management, and urban planning. Polarimatric SAR (PolSAR) system that acquires multiband and quad-polarized radar scatter is superior to other SAR systems in terms of characterizing land-cover types. In recent years, many research works have been devoted to the processing of PolSAR data and have testified advantages of PolSAR systems [1]–[3]. Among various applications of PolSAR images, the differentiating of land use and land cover types based on image classification scheme has received great significance.

Traditionally, PolSAR image classification methods take image pixel as processing unit and mainly depend on the features and statistical information of the pixels. Recently, some deep representation learning-based methods [4] have been proven to have superior performance for optical images. However, the development of deep learning in PolSAR image processing is still in its infancy, due to the greediness of labeled training samples with deep learning techniques [5], [6]. In the last few decades, many pixel-based methods have been developed for the classification of PolSAR images, such as support vector machine (SVM) [7], [8], Wishart distribution [9], and neural networks [10]. These methods can preserve detail information of images and have obtained good results for the medium- and low-resolution PolSAR images. However, with regard to high-resolution images, due to high-intraclass and low-interclass variability of image pixels, pixel-based image classification algorithms often generate the salt-and-pepper result and decrease image classification accuracy [11].

One way to deal with this problem is to impose coherent spatial regularization by computing features that account for the neighborhood of an individual pixel [12]. For PolSAR images, different from polarimetric features that can only account for characteristics of an individual pixel, mathematical morphology derived from the grayscale image can provide spatial information about the size, orientation, and structures of land cover types. Since 2000, morphology has been widely applied in feature extraction [13], speckle filtering [14], and classification [15] of SAR/PolSAR images. The research works demonstrate that the introduction of image spatial information described by mathematic morphologies can significantly increase the accuracy of SAR/PolSAR image processing. Recently, numerous variations and extensions of morphology are postulated for remote sensing images [16]–[19]. The promising experimental results demonstrate the potential of extended morphologies for SAR/PolSAR images.

Another way to improve the classification accuracy of high-resolution images is developing object-based methods. This methodology is implemented on the image objects that are composed of pixels with similar characteristics [20]. Qi *et al.* [21]

Manuscript received April 3, 2019; revised July 16, 2019 and November 1, 2019; accepted January 18, 2020. Date of publication January 31, 2020; date of current version February 18, 2020. This work was supported in part by the National Natural Science Foundation of China under Grant 61871158, in part by Scientific Research Foundation for the Returned Overseas Scholars of Heilongjiang Province under Grant LC2018029, and in part by Aeronautical Science Foundation of China under Grant 20182077008. *(Corresponding authors: Lamei Zhang.)*

The authors are with the Department of Information Engineering, Harbin Institute of Technology, Harbin 150001, China (e-mail: zoubin@hit.edu.cn; fangxu_im@163.com; lmzhang@hit.edu.cn).

Digital Object Identifier 10.1109/JSTARS.2020.2968966

propose object-based PolSAR image classification using decision tree algorithms by distinguishing mean values of polarimetric features of pixels contained in image objects. Jiao *et al.* [22] construct image objects by utilizing two-level segmentation and implements a classification method with the polarimetric signature of image objects. Omati and Sahebi [23] developed a binary classification method with the ratio of mean pixel values of the corresponding image objects for PolSAR images change detection. These works have proven that object-based image classification (OBIC) methods are effective in the improvement of classification accuracy, compared to pixel-based classification methods for PolSAR images. However, these OBIC methods usually utilize the mean value of pixels included in an image object as the object description, which may cause the loss of image detail information [24].

Obtained by image segmentation processing, image objects that correspond to realistic geographic entities in the physical world contain various object-level spatial, semantic, and topological features [25]. Recently, many research works have been devoted to the investigation of various features of image objects for optical remote sensing images [26], [27]. Although these object-level features can increase the classification accuracy of optical remote sensing images, the incorporation of object-level features has not been well investigated and applied in the OBIC of PolSAR images [28]. This article investigates an object-level semantic feature to account for contextual category information between neighboring objects. And, the proposed object-level semantic feature will be combined with pixel-level features for the OBIC of PolSAR images.

In this article, a multilevel image description that consists of the proposed pixel-level spatial and object-level semantic features is developed, and their comprehensive utilization is implemented for the OBIC of PolSAR images. At the image pixel level, a multifeature and multiscale spatial description of land-cover types is proposed based on the construction of polarimetric morphological profiles (PMPs) that take advantage of both spatial and polarimetric features of image pixels. At the image object level, as a complement to the proposed pixel-level feature that accounts for the neighborhood of individual pixels, an object-based semantic indicator is developed to quantitatively describe the semantic relationship of image objects. Finally, the integration of the proposed pixel-level spatial and object-level semantic features is implemented based on the OBIC of PolSAR images.

The rest of this article is organized as follows. Section II presents details of the proposed pixel-level PMP spatial features; Section III presents the generation of the object-level semantic indicator. Then, Section IV describes the integration of pixel-level spatial and object-level semantic features for the object-based classification of PolSAR images. Section V discusses the experiments by conducting the proposed method on PolSAR images. Section VI concludes this article with some remarks and recommendations for future research.

## II. Pixel-Level Spatial Features Described by PMPs

Due to various sizes and structures of land-cover types in the physical world, analysis of PolSAR image with a unified scale is apparently not suitable. Mathematic morphology can describe the structure and spatial information of images at different scales by changing scale element and can overcome drawback of spurious extrema or intensity shifts and preserve edges of objects in SAR/PolSAR images. Extended morphological profiles (MP) [29] that can describe multiple attribute profiles of images through the combination of multiple morphological operators (MOs) can be incorporated to depict multiscale information of PolSAR images. In the meantime, due to the scattering characteristics of PolSAR mechanisms, polarimetric information plays a dominant role in the identification of land-cover types. Hence, the PMPs generated by performing extended morphological theory on selected polarimetric indicators are developed to describe pixel-level spatial features of PolSAR images.

### A. Polarimetric Indicators

Generally, traditional methods often implement mathematical morphology on grayscale images and adopt span image of PolSAR as original input to derive morphological features [18], [19]. In this article, taking into account that different land-cover types often possess different scattering characteristics, polarimetric features of PolSAR image are employed to produce polarimetric and spatial profiles. Each component obtained by target decomposition algorithms [30]–[32] can be used to describe a mode of scattering mechanism for land-cover types. Thus, the components that can describe the dominant scattering mechanisms of contents in PolSAR images are selected from the features generated by many polarimetric decomposition methods. These components are described as polarimetric indicators that will be devoted to mathematic morphology to implement the combination of polarimetric and spatial descriptions of PolSAR images for the construction of pixel-level spatial profiles.

### B. Polarimetric Morphological Profiles

The fundamental idea of MO [16] is applying a structure element (SE) $B_k$, e.g., a square window of size $k \times k$, on a grayscale image $I$. Among the mathematical morphology operators, erosion $\varepsilon$, dilation $\delta$, opening $\gamma$, and closing $\phi$ are four widely utilized operations, defined as

$$\begin{aligned}
\varepsilon_{B_k}(I) &= \bigwedge_{b \in B_k} I_{-b} \\
\delta_{B_k}(I) &= \bigvee_{b \in B_k} I_{-b} \\
\gamma_{B_k}(I) &= \delta_{B_k} \circ \varepsilon_{B_k}(I) \\
\phi_{B_k}(I) &= \varepsilon_{B_k} \circ \delta_{B_k}(I).
\end{aligned} \tag{1}$$

By sequential application of MOs with varying size $k$, MP can be generally generated. The bigger the window size $k$ is, the larger-scale information is extracted, and the more detail edges are blurred. The PMP can be developed by extending MP to the application on polarimetric indicators $F_P = [f_1, f_2, \ldots, f_m]$. The parameter $m$ denotes the number of polarimetric indicators. Essentially, according to the principle of morphology, MOs cannot be applied to polarimetric features with negative values.

Based on the variation of size parameter $k$, a series of PMP can be obtained that construct the multifeature and multiscale spatial descriptions of image objects. In this article, MP is composed of the concatenation of morphological operation erosion $\varepsilon$ and dilation $\delta$, opening $\gamma$, and closing $\phi$, denoted as $\alpha_{B_k}(f_\lambda) = \{\varepsilon_{B_k}(f_\lambda),\ \gamma_{B_k}(f_\lambda)\}$, $\beta_{B_k}(f_\lambda) = \{\delta_{B_k}(f_\lambda),\ \phi_{B_k}(f_\lambda)\}$, which are two dual MOs.

Then, the first part of PMP can be denoted as

$$AP_k(f_\lambda) = \alpha_{B_k}(f_\lambda),\ \forall \lambda \in [1,m] \text{ and } \forall k \in [0,n] \quad (2)$$

where $AP_k(f_\lambda)$ is the first part of PMP and is constructed by the MO $\alpha$ with a SE $B_k$ of size $k$ from 0 to $n$, which is applied to a feature map $f_\lambda, \lambda \in [1,m]$.

The second part of PMP can be denoted as

$$BP_k(f_\lambda) = \beta_{B_k}(f_\lambda),\ \forall \lambda \in [1,m] \text{ and } \forall k \in [0,n] \quad (3)$$

where $BP_k(f_\lambda)$ denotes the second part of PMP and is constructed by the MO $\beta$ applied on $f_\lambda$ with the SE size $k$ varying from 0 to $n$. Since MO $\alpha$ and $\beta$ are dual, the PMP composed of $AP_k(f_\lambda)$ and $BP_k(f_\lambda)$ is self-dual as

$$\begin{aligned}\text{PMP}(f_\lambda) &= AP_k(f_\lambda) \cup BP_k(f_\lambda) \\ &= \{\alpha_n(f_\lambda), \alpha_{n-1}(f_\lambda), \ldots, \alpha_1(f_\lambda), \\ &\quad f_\lambda, \beta_1(f_\lambda), \ldots, \beta_{n-1}(f_\lambda), \beta_n(f_\lambda)\}, \lambda \in [1,m]. \end{aligned} \quad (4)$$

The PMP($f_\lambda$) denotes the morphological profile applied on polarimetric indicators, which is obtained by a combination of sets $AP_k(f_\lambda)$ and $BP_k(f_\lambda)$. Actually, $AP_0(f_\lambda)$ and $BP_0(f_\lambda)$ are equal to the grayscale image $f_\lambda$.

Thus, based on the collection of feature set $F_P$ and morphological profiles MP($f_\lambda$), the multifeature and multiscale PMP with a dimensionality of $m*(2n+1)$ can be generated to provide pixel-level spatial features that consist of polarimetric and spatial information of PolSAR images. The size parameters $n$ and $m$ determine the maximum scale of image descriptions.

## III. Object-Level Semantic Features Derived From Object Adjacency Graph

Apart from pixel-level spatial features, based on the construction of the image object adjacency graph (OAG), a novel object-level semantic indicator that describes the object-level semantic information of neighboring objects is proposed. Image objects acquired from image segmentation are segments that consist of pixels with similar or same characteristics and correspond to entities in the real world. The greatest superiority of object-based image analysis compared to pixel-based image analysis is that OBIC can take advantage of object-level spatial, semantic, and topological features of image objects for the classification of PolSAR images.

### A. Construction of OAG

The OAG is often generated by some image segmentation procedure. In this article, mean-shift algorithm [33] that clusters pixels by a moving window is first adopted to generate initial segments set $S$ of PolSAR images. These segments $s_i \in S$ are usually oversegmented and cannot separately represent an image objects that correspond to entities on the ground. Therefore, based on these initial segments $s_i$, a region-merging strategy [34] is implemented to construct the OAG that contains spatial, semantic, and topological relationships of object neighborhood.

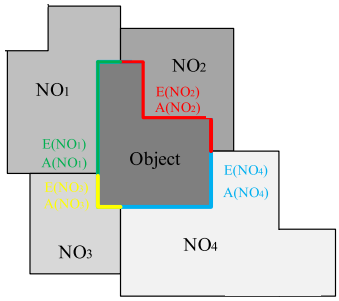


Fig. 1. Exemplified scheme for the object-level semantic indicator.

Essentially, for the construction of OAG, the region-merging strategy identifies the scale of image objects and conducts the merging process under the guidance of heterogeneity measurement $H$ and scale criterion $D$, denoted as follows:

$$\text{OAG} = \Big\{ O_i | \operatorname{scale}(O_i) \geq D^2 \cap \|s_m - s_n\|^2 \leq H, \\ s_m, s_n \in S, i \leq N \Big\} \quad (5)$$

where OAG denotes the object adjacency graph that is composed of image objects and $N$ represents the number of image objects in OAG; $s_m$ and $s_n$ represent image segments in set $S$ that are produced by mean shift segmentation; $\|s_m - s_n\|^2$ represents distances of the polarimetric features of segments $s_m$ and $s_n$, and scale($O_i$) calculates the number of pixels contained in the object $O_i$ and the threshold $D$ controls the minimum scale of image objects. The threshold $H$ evaluates the heterogeneity between image segments

PolSAR image objects in the OAG have high-interclass and low-intraclass heterogeneity. They possess meaningful spatial scales that are controlled by parameters $H$ and $D$. The higher $H$ and $D$ will lead to larger-scale image objects that consist of more segments which may result in oversegmentation, and the smaller $H$ and $D$ will result in smaller scale image objects that consist of fewer segments which may cause undersegmentation.

### B. Object-Level Semantic Indicator for PolSAR Image

In compensation for a pixel-level spatial feature that can only provide local information of image pixels, an object-level feature that can describe the semantic relationship of image objects is developed in this part. Based on initial labeling information of image pixels, the proposed object-level semantic indicator incorporates both region area and common edges of neighboring objects to account for the contextual relationship between neighboring objects based on OAG.

The exemplified scheme, as shown in Fig. 1 presents several adjacent objects of various sizes and shapes in OAG. Assume $\text{NO}_j$ represents the $j$th neighboring objects of the object $O$, $E(\text{NO}_j)$ is the length of common edge, and $A(\text{NO}_j)$ is the region area, $P$ represents the initial labeled image pixels,

$N(P \in \omega_l \cap P \in \mathrm{NO}_j)$ represents the number of pixels in object $\mathrm{NO}_j$ that is assigned to $l$th class $\omega_l$, where $l$ takes value from the class set $\Lambda = \{1, 2, \ldots, L\}$, and $L$ represents the number of classes in the image. The proposed semantic indicator $R_{O\in\omega_l}$ is defined as follows:

$$R_{O\in\omega_l} = \sum_{\mathrm{NO}_j \in \mathrm{NO}} \frac{E(\mathrm{NO}_j) N\left(P \in \omega_l \cap P \in \mathrm{NO}_j\right)}{A(\mathrm{NO}_j)}, \quad l \in \Lambda. \tag{6}$$

Generally, it is often difficult to distinguish some land cover types at the image pixel level and may result in misclassified pixels. The proposed semantic indicator $R_{O\in\omega_l}$ quantitatively evaluates the contextual relationship between image objects and can provide object-level information for image classification. Since $E(\mathrm{NO}_j)$ can show the strength of the connection between adjacent objects and $A(\mathrm{NO}_j)$ can measure attractions among various sized regions, the influence of neighboring objects on an image object can be incorporated in the description of image objects. Additionally, though neighboring objects have common edges, they possess different region sizes and contain different category information of image pixels. Therefore, the semantic indicator $R_{O\in\omega_l}$ is directed, and neighboring objects may have different attractions on each other.

## IV. Integration of Pixel-Level and Object-Level Features for PolSAR Image Classification

The pixel-level spatial features described by PMP can provide detailed spatial information of image pixels and the object-level semantic indicator can quantitatively describe contextual information of image objects. Therefore, a multilevel image description that consists of proposed pixel-level and object-level features is developed by integrating them in the OBIC for PolSAR images. The flowchart of the OBIC scheme that incorporates the proposed spatial and semantic features (SSOBIC) is shown in Fig. 2. First, initial labeling of the PolSAR image is generated with pixel-level PMP spatial features; then, based on the construction of image OAG, the proposed object-level semantic indicator is introduced as a weighting coefficient in a majority voting (MV) strategy to regularize the image initial labels and obtain the OBIC classification.

### A. Initial Labeling of PolSAR Image With Pixel-Level PMP Spatial Features

In the initial labeling procedure of PolSAR images, the proposed pixel-level spatial feature that combines both polarimetric and morphological profiles is incorporated in a pixel-based classification algorithm to generate initial labels with higher accuracy. Since the initial labeling procedure generates the category information of image pixels, it has a great influence on the accuracy of the derivation of OBIC result [35], [36].

For the construction of PMP proposed in Section II, each component in the polarimetric feature space is a grayscale image that describes a dominant physical scattering mode of land-cover types in the PolSAR system, and the profiles generated by a series of spatial element construct the multiscale morphological description of various land-cover types. The constructed pixel-level PMP spatial features will be devoted to a pixel-based classification algorithm as shown in Fig. 2. The SVM with Gaussian radial basis function (SVM-RBF) is incorporated in this article to perform the initialing labeling of image pixels. It uses a certain distance between samples as the criterion of classification and maps the sample features into high-dimensional space [37]. The penalty coefficient $c$ and kernel parameter $\gamma$ are two dominant parameters that control the ability of kernel in fitting the nonlinear characteristics of PolSAR data, and their values are determined by the grid searching strategy that inherent in PolSARpro software.

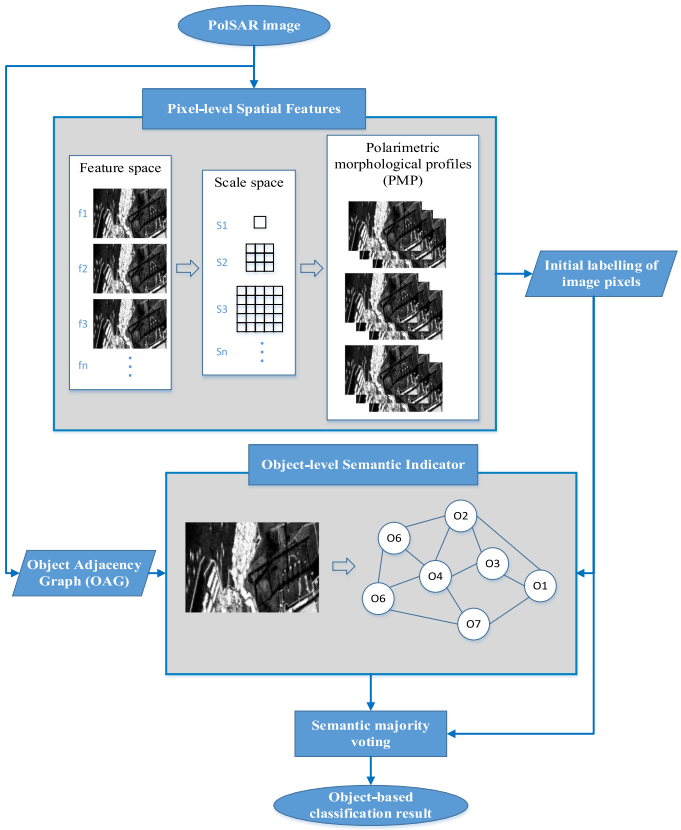


Fig. 2. Framework of the proposed SSOBIC method.

### B. Regularization of Image Initial Labels With Object-Level Semantic Indicator

The generation of preliminary pixel labels by the pixel-based classification procedure only considers the local spatial relationship of an individual pixel, while the construction of OAG can provide adaptive spatial and semantic information of image object neighborhood. Therefore, based on the derived initial pixel labels and constructed OAG, the proposed object-level semantic indicator $R_{O\in\omega_l}$ is incorporated as a weighted coefficient in the MV procedure to assign a unified label for the pixels included in an object. Assuming $N(P \in \omega_l \cap P \in O)$ represents the number of pixels $P$ assigned to class $\omega_l$ in the

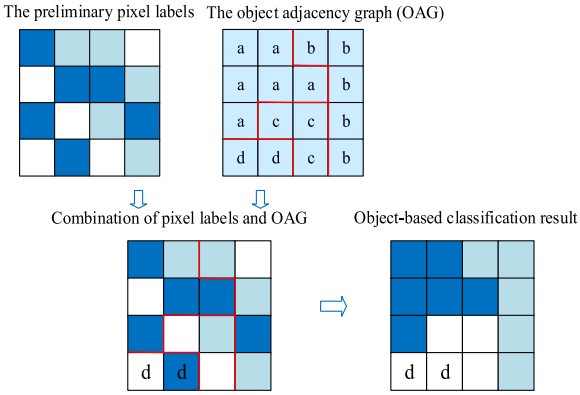


Fig. 3. Exemplified framework for the generation of object-based classification based on semantic weighted MV.

object $O$, the object $O$ will be classified into class $\omega_i,\ i \in \Lambda$, if

$$\omega_i = \arg\max_{l \in L} \left( N\left(P \in \omega_l \cap P \in O\right) + R_{O \in \omega_l} \right). \quad (7)$$

In this way, the proposed semantic indicator that describes contextual information of image objects is incorporated in the MV strategy. The contextual object-based reclassification is shown in Fig. 3.

As illustrated in Fig. 3, each $4 \times 4$ grid represents an image and small boxes represent image pixels. In the initial labeling image, the boxes with three different colors represent image pixels assigned to three different classes derived by pixel-based classification. In the OAG image, the letters "a," "b," "c," and "d" represent four different image objects produced by image segmentation procedure. In the combined initial labels and OAG image, the red lines separate four image objects according to OAG. In the traditional MV strategy, the label of object $O_i$ is determined only by pixels included in it. In this article, on image object level, the semantic indicator proposed in Section III that accounts for the information of neighboring objects $NO_j$ of object $O$ is incorporated in MV procedure.

Taking the image object represented by "d" as an example, the two pixels belonged to image object "d" are initially categorized into two different classes masked by white and blue colors, respectively. It may be dilemmatic to determine the label of this object by the traditional MV strategy. By considering contextual information in neighborhood objects that quantify by the proposed semantic indicator, the object "d" is assigned to the class that is masked by white color. Through overlapping the classification and segmentation maps, the proposed SSOBIC scheme can take advantage of both pixel-level spatial and object-level semantic features for the classification of high-resolution PolSAR images.

## V. Experimental Results and Discussion

The experimental analysis is performed on two different airborne fully polarized SAR images. The first data set was acquired over the area of Oberpfaffenhofen, Germany, by the L-band ESAR sensor, with a resolution of $3 \times 3$ m. The selected test image is made up of 1300 pixels in lines and 1200 pixels in columns, covering the airport runways of Oberpfaffenhofen. The second

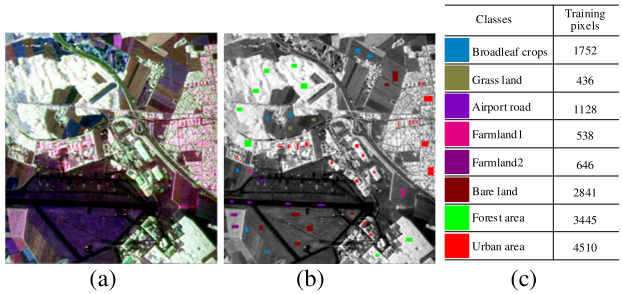


Fig. 4. ESAR data set. (a) Pseudo color image. (b) Groundtruth image. (c) Number of training sample pixels.

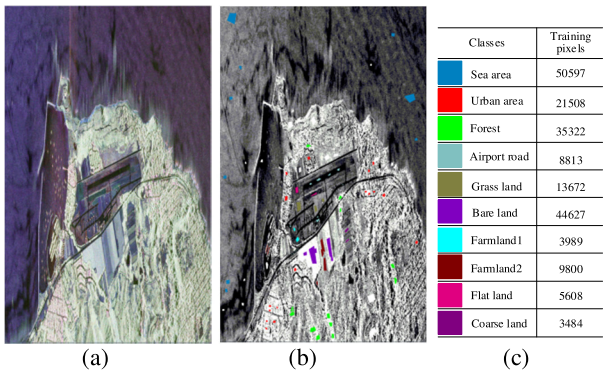


Fig. 5. UAVSAR data set. (a) Pseudo color image. (b) Groundtruth image. (c) Number of training sample pixels.

data set was acquired over the area of a harbor in San Francisco, USA, by the L-band uninhabited airborne vehicle synthetic aperture radar (UAVSAR) with a resolution of $0.7 \times 1.6$ m. The adopted test image is composed of $3377 \times 5501$ pixels.

### A. Datasets and Experimental Setup

By setting the intensities of double-bounce scattering, volume scattering, and odd-bounce scattering as red, green, and blue components, respectively, the pseudo color image of Pauli decomposition for ESAR and UAVSAR images can be obtained, as shown in Figs. 4(a) and 5(a), respectively. The pseudo-color image can give a distinct description of these two test areas. The ESAR test image can be categorized into eight classes: grass land, airport roads, forest area, urban area, bare land, and three kinds of farmlands. The UAVSAR test image mainly contains ten semantic land cover types: sea area, forest area, urban area, airport road, grassland, terrace, flat land, coarse land, farmland1, and farmland2. The selection of sample pixels is marked in Fig. 4(b) and (b) by different colors, the number of selected training sample pixels are shown in Fig. 4(c) and (c), respectively.

For both images, the multifeature and multiscale morphological profiles are constructed. By verifying different combinations of polarimetric features, four parameters of Yamaguchi decomposition are selected as the polarimetric indicators. They are feature images $f_{\text{odd}}$, $f_{\text{dbl}}$, $f_{\text{vol}}$, and $f_{\text{hlx}}$ that describe the odd-bounce, double-bounce, volume, and helix scattering characteristics of land-cover types, respectively. The sets of mixed MOs

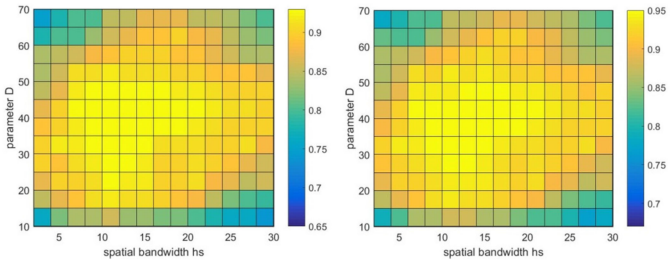


Fig. 6. Quantitative evaluation of the proposed method with different parameters $D$ and $h_s$. (a) Kappa index. (b) OA.

have yielded satisfactory results in previous works. Hence, in this article, erosion $\varepsilon$ and dilation $\delta$, opening $\gamma$ and closing $\phi$ are all adopted to form the multiscale morphological profiles based on a square-shaped element with linear increasing size (i.e., 1, 3, 5 and 7).

In the pixel-based classification procedure, Gaussian RBF is selected as the kernel function of SVM algorithm, and the penalty coefficient $c$ and kernel parameter $\gamma$ in the procedure are optimized based on the grid searching strategy by PolSARpro software [38]. Regarding the generation of preliminary image segments, the mean shift algorithm is used to segment the intensity image $I$ first. The selection of kernel function plays an important role in MS segmentation. In this article, a typical Gaussian kernel function is employed as it models density as a smooth function. In the segmentation procedure, the spatial domain bandwidth $h_s$ and pixel similarity threshold $h_r$ jointly control the magnitude and the orientation of the mean shift vector. The higher values of $h_s$ and $h_r$ can include more pixels in the processing range and reduce more speckle-noise inherent in PolSAR images, while it may smooth the detailed edges of land cover types. In all the comparative studies, range bandwidth is set as $h_r = 8$ by empirical experiments for intensity images. As to the construction of image objects, in the region-merging procedure, the heterogeneity coefficient $H$ [34] is calculated as $H = \omega\sqrt{\sum_{l=1}^{L}\omega_l {\sigma_l}^2} + (1-\omega)[(1-\omega_s)\frac{c}{r} + \omega_s\frac{c}{\sqrt{n}}]$, in which $L = 3$ is the number of adopted polarimetric features; $c$, $n$, and $r$ are the perimeter, pixel number, and external rectangle area of image objects, respectively; the shape coefficient $\omega_s$ and weight parameters $\omega$ and $\omega_l$ are set as $\omega_s = 0.5, \omega = 0.2$, and $\omega_l = 1$ for ESAR image and set as $\omega_s = 0.5$, $\omega = 0.4$, and $\omega_l = 1$ for UAVSAR image by empirical experiments. The spatial bandwidth $h_s$ in mean-shift segmentation determines the analysis scale in spatial domain, and the threshold $D$ describes the size of image objects which indicates that the minimum number of pixels contained in object is larger than $D^2$ in region-merging process.

Since both $h_s$ and $D$ determine the segmentation scale, an experiment is implemented on the ESAR image to evaluate their sensitivity in the proposed method. By setting the values of spatial bandwidth $h_s$ from 2 to 30 with step 2 and parameter $D$ from 10 to 70 with step 5, the overall accuracy (OA) and the kappa index ($K$) [39], [40] of classification results are shown in Fig. 6. The higher values of OA and $K$ indicate higher classification accuracy and more satisfactory results. It can be found that approximate optimal results can be obtained when $h_s$ is within the range (6–22) and the parameter $D$ is set within (25–60). Since both intervals are quite long, the proposed method is robust to the selection of $h_s$ and $D$.

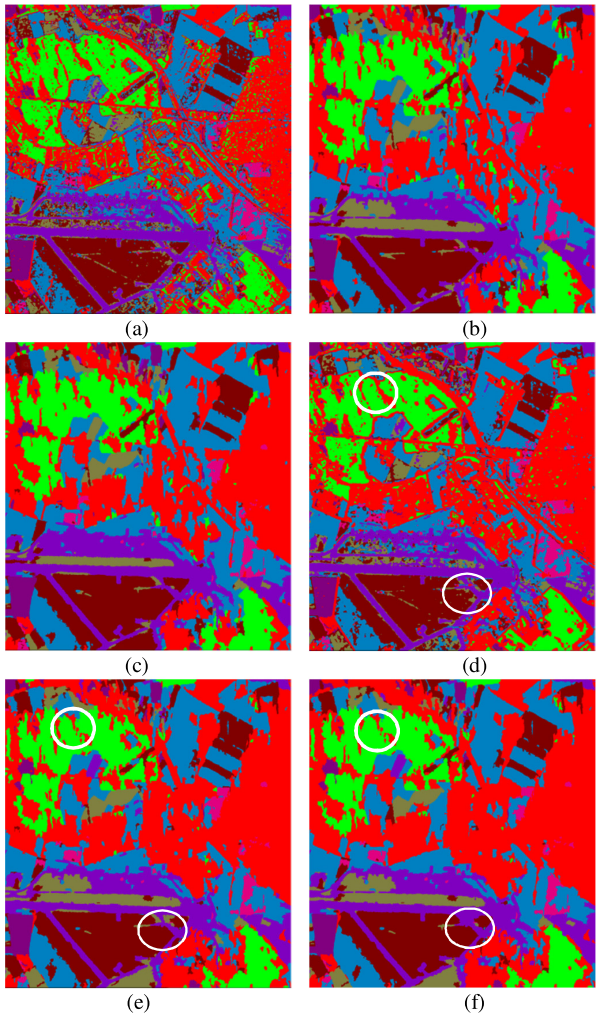


Fig. 7. Classification result of ESAR data. (a) SVM classification of polarimetric features. (b) MV classification of polarimetric features. (c) Semantic_MV classification of polarimetric features. (d) SVM of PMP features. (e) MV of PMP features. (f) Semantic_MV of PMP features. With $\omega_s = 0.5, \omega = 0.2$, $\omega_l = 1$, and $D = 40$.

### B. Classification of the ESAR Image

The proposed pixel-level spatial and object-level semantic features are both evaluated. To testify the effectiveness of PMPs, classification methods are performed on polarimetric features of the Yamaguchi decomposition algorithm and the proposed PMPs, respectively. The proposed OBIC scheme based on semantic MV (semantic_MV) is compared with the traditional MV strategy and pixel-based classification results of the SVM algorithm.

Fig. 7 displays the classification results, and Tables I and II list the producers' and users' accuracies of eight categories, OA, and $K$. Fig. 7(a) and (d) are the SVM classification results based on polarimetric features and PMP, respectively. Comparing these

TABLE I
PRODUCERS' ACCURACY OF DIFFERENT METHODS FOR THE ESAR DATA SET

| Feature vector | Classification method | Producer's accuracy of classification (%) | | | | | | | | OA(%) | Kappa |
|---|---|---|---|---|---|---|---|---|---|---|---|
| | | Broad leaf crops | Grass land | Airport roads | Farm1 | Farm2 | Bare land | Forest area | Urban area | | |
| Polarimetric features | SVM | 93.86 | 83.12 | 99.75 | 82.48 | 98.96 | 95.34 | 80.90 | 82.63 | 89.20 | 0.87 |
| | MV | 97.56 | 96.47 | 98.83 | 80.06 | 100 | 97.33 | 81.43 | 88.86 | 92.20 | 0.90 |
| | Semantic_MV | 98.00 | 96.47 | 99.93 | 83.32 | 100 | 99.14 | 83.29 | 90.82 | 93.67 | 0.92 |
| PMP | SVM | 95.31 | 85.54 | 99.92 | 86.62 | 98.32 | 95.91 | 83.85 | 94.14 | 92.70 | 0.91 |
| | MV | 96.48 | 96.35 | 98.83 | 86.92 | 100 | 97.21 | 82.07 | 96.03 | 93.69 | 0.92 |
| | Semantic_MV | 98.10 | 97.27 | 98.83 | 88.92 | 100 | 99.34 | 85.11 | 96.46 | 95.25 | 0.94 |

TABLE II
USERS' ACCURACY OF DIFFERENT METHODS FOR THE ESAR DATA SET

| Feature vector | Classification method | User's accuracy of classification (%) | | | | | | | | OA(%) | Kappa |
|---|---|---|---|---|---|---|---|---|---|---|---|
| | | Broad leaf crops | Grass land | Airport roads | Farm1 | Farm2 | Bare land | Forest area | Urban area | | |
| Polarimetric features | SVM | 89.33 | 93.80 | 92.57 | 83.65 | 91.81 | 95.42 | 87.31 | 80.84 | 89.20 | 0.87 |
| | MV | 89.80 | 93.69 | 89.89 | 80.48 | 99.84 | 98.88 | 95.78 | 82.75 | 92.20 | 0.90 |
| | Semantic_MV | 91.09 | 95.42 | 89.99 | 100 | 99.84 | 99.26 | 97.03 | 84.75 | 93.67 | 0.92 |
| PMP | SVM | 93.23 | 96.72 | 93.36 | 86.29 | 95.70 | 96.45 | 94.91 | 85.12 | 92.70 | 0.91 |
| | MV | 94.91 | 94.62 | 89.89 | 84.52 | 96.61 | 98.77 | 99.06 | 84.27 | 93.69 | 0.92 |
| | Semantic_MV | 96.51 | 95.84 | 92.12 | 95.63 | 97.90 | 99.34 | 99.55 | 86.43 | 95.25 | 0.94 |

two maps, it can be seen that there are many misclassified small patches in Fig. 7(a) and (d) are obviously more homogeneous than Fig. 7(a). From Table I, OA of pixel-based classification based on PMP is superior to OA based on only polarimetric features by 3.5% and the $K$ is improved by 0.4. The reason may be that the traditional pixel-based classification method takes image pixel as a processing unit and cannot take advantage of spatial information of PolSAR images. In addition, polarimetric features generated by target decomposition algorithms often generate confusion between different categories due to the scattering characteristics of complex land cover types. The multiscale and multifeature morphological profiles derived from polarimetric features can provide spatial features of images and preserve the detailed information in the meantime.

Fig. 7(b) and (e) are the object-based classification results based on MV. Comparing Fig. 7(a), (b), (d), and (e), it can be found out that many small misclassified patches are removed by combining the pixel-based classification result with segmentation result. In Table I, the OA of the PMP_MV method is improved by 0.99% compared with the PMP_SVM method, and the OA of the polarimetric_MV method is improved by 3.0% compared with polarimetric_SVM method. The cause of this phenomenon may be that the segmentation map provides edge information and homogeneous regions for object-based classification. Hence, the classification accuracies can be relatively improved. However, the traditional MV strategy only considers the pixels included in the object that may results in misclassifications of the object.

Fig. 7(c) and (f) are the proposed object-based classification results based on semantic MV. By incorporating the semantic information in the voting strategy, the OA can be further improved compared with that of the MV result. The misclassified forest area and broadleaf crop regions in Fig. 7(e) are correctly classified in Fig. 7(f), marked by white circles. Based on PMP feature space, when traditional MV strategy is adopted, the classification accuracy of the forest area is decreased by 1.78% compared to the SVM classification. However, compared to SVM classification, the accuracy of forest area can be improved by 1.26% with the Semantic_MV method. This improvement is due to the fact that the contextual information of image objects is considered and, thus, providing more reliable information in the determination of object categories. The experimental results validate that the proposed method can obtain the more satisfying result by incorporating the semantic information.

Tables I and II display the producers' and users' accuracy of different methods for ESAR image, respectively. Based on the combination of pixel-level and object-level features, the proposed method can obtain satisfactory results in distinguishing different land-cover types, with an OA of 95.25% and the $K$ is 0.94. However, there still exist misclassifications between forest area and urban area, directly resulting in relative low producers' accuracy of forest area in Table I and low users accuracy of the urban area in Table II. As discussed in many works [41], [42], due to similar characteristics of forest and buildings in PolSAR system, it is often difficult to distinguish them in PolSAR image classification, and how to select effective polarimetric indicators is still an open problem.

### C. Classification of the UAVSAR Image

To evaluate the robustness of the proposed method, an additional high-resolution fully polarized SAR image with a resolution of 0.7 $\times$ 1.6 m is adopted in this article. The UAVSAR image is acquired by an L-band airborne sensor covering a harbor area in San Francisco of the USA. In this experiment, the image is categorized into ten classes: sea area, urban area, forest area, airport road, grass land, terrace, farmland1, farmland2, flat land, and coarse land.

Fig. 8 displays the UAVSAR classification results, and Tables III and IV list the producers' and users' accuracies of ten categories, OA, and kappa index that denoted as $K$. Fig. 8(a)–(c) are classification results based on polarimetric features and denote the pixel-based classification (SVM), OBIC based on MV strategy, and Semantic_MV classification results, respectively. Fig. 8(d)–(f) are the classification results based on the PMP features, and they are the pixel-based classification result and object-based classification results based on MV and based on Semantic_MV, respectively.

Comparing Fig. 8(a) and (d), it can be found that there is a mass of salt-and-pepper in Fig. 8(a), while Fig. 8(d) is more homogeneous. Referring to Table III, the classification OA of Fig. 8(d) is higher than Fig. 8(a) by 8.09%. This is mainly benefited by the incorporation of polarimetric and morphological spatial profiles. Since similar scattering characteristics of different land cover types may cause confusion during the pixel-based classification procedure, the MP features provide multiscale spatial, and structure information of objects, which can improve the classification accuracy and generate more homogeneous classification results. Referring to Fig. 8(c), there are more misclassified small patches comparing to Fig. 8(f), though the OA is improved compared to the pixel-based classification result in Fig. 8(a) and (b). Since the main difference between these two methods is the features incorporated in the pixel-based classification procedure, it demonstrates that the proposed method depends on the pixel-based classification result to some extent.

Fig. 8(e) displays the object-based classification result based on traditional MV, and Fig. 8(f) is the classification result based on Semantic_MV strategy proposed in this article. Comparing the area circled by white rectangles in these images, we can find that many sea area pixels that misclassified in Fig. 8(d) are mostly removed in Fig. 8(e), but still remain several misclassified small patches. These misclassified patches are completely removed and the classification accuracy is further improved in Fig. 8(f), which incorporates the object-level semantic information. Referring to Table III, the classification

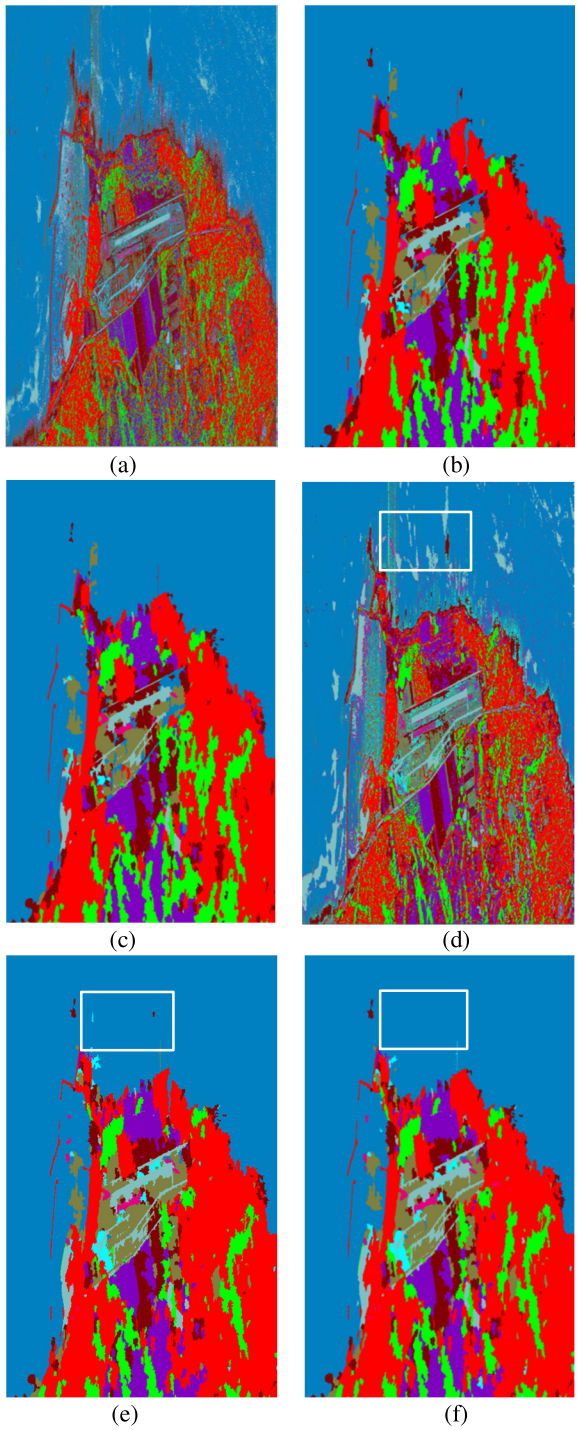


Fig. 8. Classification result of UAVSAR data. (a) SVM classification of polarimetric features. (b) MV classification of polarimetric features. (c) Semantic_MV classification of polarimetric features. (d) SVM of PMP features. (e) MV of PMP features. (f) Semantic_MV of PMP features. With $\omega_s = 0.5, \omega = 0.4, \omega_l = 1$, and $D = 55$.

TABLE III
PRODUCERS' ACCURACY OF DIFFERENT METHODS FOR THE UAVSAR DATA SET

| Feature vector | Classification method | Producer's accuracy of classification (%) | | | | | | | | | | OA (%) | K |
|---|---|---|---|---|---|---|---|---|---|---|---|---|---|
| | | Sea area | Urban area | Forest area | Airport road | Grass land | Bare land | Farm1 | Farm2 | Flat land | Coarse land | | |
| Polarimetric features | SVM | 96.40 | 72.12 | 69.60 | 76.60 | 72.29 | 91.35 | 68.13 | 88.06 | 71.69 | 74.35 | 77.04 | 0.72 |
| | MV | 100 | 94.43 | 77.80 | 72.63 | 98.87 | 87.56 | 71.53 | 90.44 | 87.35 | 78.29 | 85.84 | 0.83 |
| | Semantic_MV | 100 | 99.46 | 86.72 | 85.93 | 98.87 | 98.70 | 83.66 | 91.46 | 89.35 | 80.13 | 89.45 | 0.87 |
| PMP | SVM | 97.96 | 75.92 | 72.73 | 97.70 | 83.84 | 94.61 | 76.40 | 98.42 | 79.37 | 78.87 | 85.13 | 0.83 |
| | MV | 100 | 95.36 | 74.94 | 83.96 | 98.87 | 98.66 | 99.10 | 91.46 | 79.48 | 90.22 | 91.05 | 0.89 |
| | Semantic_MV | 100 | 99.46 | 85.92 | 87.95 | 100 | 98.70 | 99.10 | 92.07 | 80.90 | 93.01 | 92.50 | 0.91 |

TABLE IV
USERS' ACCURACY OF DIFFERENT METHODS FOR THE UAVSAR DATA SET

| Feature vector | Classification method | User's accuracy of classification (%) | | | | | | | | | | OA (%) | K |
|---|---|---|---|---|---|---|---|---|---|---|---|---|---|
| | | Sea area | Urban area | Forest area | Airport road | Grass land | Bare land | Farm1 | Farm2 | Flat land | Coarse land | | |
| Polarimetric features | SVM | 93.35 | 81.10 | 78.71 | 76.35 | 94.88 | 66.68 | 74.15 | 88.70 | 70.20 | 93.42 | 77.04 | 0.72 |
| | MV | 99.71 | 79.65 | 96.46 | 73.93 | 73.95 | 74.02 | 99.98 | 88. 89 | 79.15 | 98.93 | 85.84 | 0.83 |
| | Semantic_MV | 99.00 | 100 | 99.60 | 84.82 | 80.23 | 76.96 | 100 | 87.08 | 87.28 | 98.95 | 89.45 | 0.87 |
| PMP | SVM | 81.50 | 77.80 | 78.19 | 89.51 | 66.40 | 90.06 | 89.41 | 90.15 | 85.42 | 78.47 | 85.13 | 0.83 |
| | MV | 100 | 90.46 | 96.18 | 81.30 | 78.60 | 83.31 | 95.86 | 97.95 | 88.94 | 100 | 91.05 | 0.89 |
| | Semantic_MV | 100 | 93.09 | 87.43 | 83.55 | 87.38 | 92.76 | 99.87 | 93.89 | 100 | 100 | 92.50 | 0.91 |

accuracy is improved by 1.45% when the semantic information between neighboring objects is taken into consideration during the definition of the label for each object. Hence, the combination of semantic features and object-based classification framework can further improve the classification accuracy.

Tables III and IV display the producers' and users' accuracy of different methods for the UAVSAR image, respectively. There is a phenomenon need to be pointed out, the proposed method achieves the highest OA while generates the relatively low accuracy in airport road in Table III, and the users accuracy in airport road of the proposed method in Table IV is also relatively low compared to other land-cover types. The reason may be that since the PMP features are generated by combining polarimetric features and morphological features, the PMPs derived under a square window with a size of $k \times k$ may cause the detail information loss and blur the edges of the airport road.

### *D. Comparison of Low- and High-Resolution PolSAR Image Classification Results*

Comparing the classification results of ESAR image and UAVSAR image that possess different resolutions, the effectiveness of the proposed method for low- and high-resolution PolSAR images is evaluated. From Figs. 7 and 8 Tables I, and III, we can find that the OA of the low-resolution image is improved by 6.05% from 89.20% in Fig. 7(a) to 95.25% in Fig. 7(f) by incorporating the integrated pixel-level and object-level features; while, the OA of the high-resolution image is improved by 15.21% from 77.04% in Fig. 8(a) to 92.25% in Fig. 8(f). Therefore, the proposed integrated utilization of pixel-level spatial and object-level semantic features in object-based image analysis can more effectively improve the classification accuracy for high-resolution images comparing to low-resolution images. The cause may be that high-resolution PolSAR images contain more abundant spatial, semantic, and topological information than low-resolution PolSAR images. However, comparing the OA of these PolSAR images with different resolutions, the classification accuracy of the high-resolution image is relatively lower than the low-resolution image, this may be caused by the more complex information contained in high-resolution PolSAR images that has resulted in high heterogeneity in intraclass and high homogeneity in interclass. Based on the comparison of low-resolution and high-resolution images, it can be found that the proposed OBIC that takes advantages of the proposed integration of pixel-level spatial and object-level semantic features can effectively improve the classification accuracy of high-resolution PolSAR images.

## VI. Conclusion

To improve the classification accuracy of high-resolution PolSAR images, a novel OBIC scheme that integrates the pixel-level spatial and object-level semantic information is proposed in this article. Based on a semantic weighted majority strategy, a pixel-based classification result is combined with the segmentation results. The innovation of the proposed method is developing a multilevel image description that consists of the proposed pixel-level spatial features described by PMPs and object-level semantic indicator derived from OAG, by integrating them in the OBIC of high-resolution PolSAR images. The fully polarized image data sets acquired from high-resolution UAVSAR and low-resolution ESAR airborne systems are adopted and compared to validate the effectiveness of the proposed method. The experiment results have proven that the spatial and semantic features adopted in this article can generate more homogeneous classification results and improve the classification accuracy for both high- and low-resolution PolSAR images. The impact of square-window-based feature extraction methods on the detail edges preservation of realistic objects can be investigated, and similar to many object-based classification methods, the proposed classification scheme depends on the performance of segmentation results.

## References


[1] J. C. Souyris, C. Henry, and F. Adragna, "On the use of complex SAR image spectral analysis for target detection: Assessment of polarimetry," *IEEE Trans. Geosci. Remote Sens.*, vol. 41, no. 12, pp. 2725–2734, Dec. 2003.

[2] C. Liuand and C. H. Gierull, "A new application for PolSAR imagery in the field of moving target indication/ship detection," *IEEE Trans. Geosci. Remote Sens.*, vol. 45, no. 11, pp. 3426–3436, Nov. 2007.

[3] J. S. Lee, M. R. Grunes, and E. Pottier, "Quantitative comparison of classification capability: Fully-polarimetric versus dual and single-polarization SAR," *IEEE Trans. Geosci. Remote Sens.*, vol. 39, no. 11, pp. 2343–2351, Nov. 2001.

[4] Y. Lecun, Y. Bengio, and G. Hinton, "Deep learning," *Nature*, vol. 521, pp. 436–444, 2015.

[5] Y. Zhou, H. Wang, F. Xu, and Y. Jin, "Polarimetric SAR image classification using deep convolutional neural networks," *IEEE Geosci. Remote Sens. Lett.*, vol. 13, no. 12, pp. 1935–1939, Dec. 2016.

[6] H. Liu, S. Yang, and S. Gou, "Polarimetric SAR feature extraction with neighborhood preservation-based deep learning," *IEEE J. Sel. Topics Appl. Earth Observ. Remote Sens.*, vol. 10, no. 4, pp. 1456–1466, Apr. 2017.

[7] S. Fukuda and H. Hirosawa, "Polarimetric SAR image classification using support vector machine," *IEICE Trans. Electron.*, vol. E84-C, pp. 1939–1945, 2001.

[8] C. Lardeux *et al.*, "Support vector machine for multifrequency SAR polarimetric data classification," *IEEE Trans. Geosci. Remote Sens.*, vol. 47, no. 12, pp. 4143–4152, Dec. 2009.

[9] J. S. Lee, M. R. Grunes, and R. Kwok, "Classification of multi-look polarimetric SAR imagery based on complex Wishart distribution," *Int. J. Remote Sens.*, vol. 15, no. 11, pp. 2299–2311, 1994.

[10] Y. Hara, R. G. Atkins, S. H. Yueh, R. T. Shin, and J. A. Kong, "Application of neural networks to radar image classification," *IEEE Trans. Geosci. Remote Sens.*, vol. 32, no. 1, pp. 100–109, Jan. 1994.

[11] J. Zhu, X. Fan, H. Guo, C. Wang, J. Tan, and X. Du, "Information extraction from high-resolution SAR image with object-oriented method," *Proc. SPIE*, vol. 7841, 2010, Art. no. 78410M.

[12] D. Tuia, F. Pacifici, M. Kanevski, and W. J. Emery, "Classification of very high spatial resolution imagery using mathematical morphology and support vector machines," *IEEE Trans. Geosci. Remote Sens.*, vol. 47, no. 11, pp. 3866–3879, Nov. 2009.

[13] B. Zou, C. Wang, C. Wang, and L. Zhang, "Coastline detection based on polarimetric characteristics and mathematical morphology using PolSAR images," in *Proc. IEEE Int. Geosci. Remote Sens. Symp.*, 2017, pp. 4562–4565.

[14] A. Alonso-González, C. López-Martínez, and P. Salembier, "Variable local weight filtering for PolSAR data speckle noise reduction," in *Proc. IEEE Int. Geosci. Remote Sens. Symp.*, 2012, pp. 2133–2136.

[15] P. R. Marpu, K. Chen, C. Chu, and J. A. Benediktsson, "Spectral-spatial classification of polarimetric SAR data using morphological profiles," in *Proc. 3rd Int. Asia-Pac. Conf. Synthetic Aperture Radar*, 2011, pp. 1–3.

[16] P. Soille, *Morphological Image Analysis: Principles and Applications*, 2nd ed. Berlin, Germany: Springer-Verlag, 2004.

[17] D. Tuia, F. Pacifici, M. Kanevski, and W. J. Emery, "Classification of very high spatial resolution imagery using mathematical morphology and support vector machines," *IEEE Trans. Geosci. Remote Sens.*, vol. 47, no. 11, pp. 3866–3879, Nov. 2009.

[18] A. Masjedi, M. J. Valadan Zoej, and Y. Maghsoudi, "Classification of polarimetric SAR images based on modeling contextual information and using texture features," *IEEE Trans. Geosci. Remote Sens.*, vol. 54, no. 2, pp. 932–943, Feb. 2016.

[19] L. Zhang, W. Ma, and D. Zhang, "Stacked sparse autoencoder in PolSAR data classification using local spatial information," *IEEE Geosci. Remote Sens. Lett.*, vol. 13, no. 9, pp. 1359–1363, Sep. 2016.

[20] T. Blaschke and G. J. Hay, "Object-oriented image analysis and scale-space: Theory and methods for modeling and evaluating multi-scale landscape structure," *Int. Archives Photogramm. Remote Sens.*, vol. 34, no. 4, pp. 22–29, 2001.

[21] Z. Qi, A. G.-O. Yeh, X. Li, and Z. Lin, "A novel algorithm for land use and land cover classification using RADARSAT-2 polarimetric SAR data," *Remote Sens. Environ.*, vol. 118, pp. 21–39, 2012.

[22] X. Jiao*et al.*, "Object-oriented crop mapping and monitoring using multi-temporal polarimetric RADARSAT-2 data," *ISPRS J. Photogramm. Remote Sens.*, vol. 96, pp. 38–46, 2014.

[23] M. Omati and M. R. Sahebi, "Change detection of polarimetric SAR images based on the integration of improved watershed and MRF segmentation approaches," *IEEE J. Sel. Topics Appl. Earth Observ. Remote Sens.*, vol. 11, no. 11, pp. 4170–4179, Nov. 2018.

[24] X. Ma, H. Shen, J. Yang, L. Zhang, and P. Li, "Polarimetric-spatial classification of SAR images based on the fusion of multiple classifiers," *IEEE J. Sel. Topics Appl. Earth Observ. Remote Sens.*, vol. 7, no. 3, pp. 961–971, Mar. 2014.

[25] T. Blaschke, "Object based image analysis for remote sensing," *ISPRS J. Photogramm. Remote Sens.*, vol. 65, pp. 2–16, 2009.

[26] P. Zhang, Z. Lv, and W. Shi, "Object-based spatial feature for classification of very high resolution remote sensing images," *IEEE Geosci. Remote Sens. Lett.*, vol. 10, no. 6, pp. 1572–1576, Nov. 2013.

[27] C. Geiß, M. Klotz, A. Schmitt, and H. Taubenböck, "Object-based morphological profiles for classification of remote sensing imagery," *IEEE Trans. Geosci. Remote Sens.*, vol. 54, no. 10, pp. 5952–5963, Oct. 2016.

[28] X. Xu, B. Zou, and L. Zhang, "Polsar image classification based on polarimetric object-based morphological profiles," in *Proc. IEEE Int. Geosci. Remote Sens. Symp.*, 2017, pp. 3270–3273.

[29] M. Dalla Mura, J. A. Benediktsson, B. Waske, and L. Bruzzone, "Morphological attribute profiles for the analysis of very high resolution images," *IEEE Trans. Geosci. Remote Sens.*, vol. 48, no. 10, pp. 3747–3762, Oct. 2010.

[30] Y. Yamaguchi, T. Moriyama, M. Ishido, and H. Yamada, "Four-component scattering model for polarimetric SAR image decomposition," *IEEE Trans. Geosci. Remote Sens.*, vol. 43, no. 8, pp. 1699–1706, Aug. 2005.

[31] J. Yang, Y. N. Peng, Y. Yamaguchi, and H. Yamada, "On Huynen's decomposition of a Kennaugh matrix," *IEEE Geosci. Remote Sens. Lett.*, vol. 3, no. 3, pp. 369–372, Jul. 2006.

[32] L. Zhang, B. Zou, H. Cai, and Y. Zhang, "Multiple-component scattering model for polarimetric SAR image decomposition," *IEEE Geosci. Remote Sens. Lett.*, vol. 5, no. 4, pp. 603–607, Oct. 2008.

[33] B. Zhang, G. Ma, Z. Zhang, and Q. Qin, "Region-based classification by combining MS segmentation and MRF for POLSAR images," *J. Syst. Eng. Electron.*, vol. 24, no. 3, pp. 400–409, Jun. 2013.

[34] U. C. Benz, P. Hofmann, G. Willhauck, I. Lingenfelder, and M. Heynen, "Multi-resolution, object-oriented fuzzy analysis of remote sensing data for GIS-ready information," *ISPRS J. Photogramm. Remote Sens.*, vol. 58, no. 3, pp. 239–258, 2004.

[35] K. Bernard, Y. Tarabalka, J. Angulo, J. Chanussot, and J. A. Benediktsson, "Spectral-spatial classification of hyperspectral data based on a stochastic minimum spanning forest approach," *IEEE Trans. Image Process.*, vol. 21, no. 4, pp. 2008–2021, Apr. 2012.
[36] M. Fauvel, Y. Tarabalka, J. A. Benediktsson, J. Chanussot, and J. C. Tilton, "Advances in spectral-spatial classification of hyperspectral images," *Proc. IEEE*, vol. 101, no. 3, pp. 652–675, Mar. 2013.
[37] V. Vapnik, *The Nature of Statistical Learning Theory*. New York, NY, USA: Springer-Verlag, 1995.
[38] L. F. Fmail and E. Pottier, *The Polarimetric SAR Data Processing and Educational Tool*. Paris, France: European Space Agency, 2005.
[39] G. M. Foody, "Thematic map comparison: Evaluating the statistical significance of differences in classification accuracy," *Photogramm. Eng. Remote Sens.*, vol. 50, no. 5, pp. 627–633, 2004.
[40] C. Goutte and E. Gaussier, "A probabilistic interpretation of precision, recall and F-score, with implication for evaluation," in *Proc. Adv. Inf. Retrieval*, 2005, vol. 3408, pp. 345–359.
[41] B. Zou, Y. Zhang, N. Cao, and N. P. Minh, "A four-component decomposition model for PolSAR data using asymmetric scattering component," *IEEE J. Sel. Topics Appl. Earth Observ. Remote Sens.*, vol. 8, no. 3, pp. 1051–1061, Mar. 2015.
[42] Y. Yamaguchi, T. Moriyama, M. Ishido, and H. Yamada, "Four-component scattering model for polarimetric SAR image decomposition," *IEEE Trans. Geosci. Remote Sens.*, vol. 43, no. 8, pp. 1699–1706, Aug. 2005.

**Bin Zou** (Senior Member, IEEE) received the B.S. degree in electronic engineering from Harbin Institute of Technology, Harbin, China, in 1990, the M.Sc. degree in space studies from International Space University, Strasbourg, France, in 1998, and the Ph.D. degree in information and communication engineering, in 2001 from Harbin Institute of Technology.

From 1990 to 2000, he was with the Department of Space Electro-Optic Engineering, Harbin Institute of Technology. From 2003 to 2004, he was a visiting scholar with the Department of Geological Sciences, University of Manitoba. He is currently a Professor and Vice Head of the Department of Information Engineering, Harbin Institute of Technology. His research interests include SAR image processing and polarimetric SAR interferometry.

**Xiaofang Xu** received the B.S. degree in electronics and communication engineering, in 2015 from Nanjing University of Aeronautics and Astronautics, Nanjing, China. She is currently working toward the Ph.D. degree in information and communication engineering at the School of Information and Communication Engineering, Harbin Institute of Technology, Harbin, China.

Her research interests include polarimetric synthetic aperture radar image interpretation including image segmentation, and classification and target detection.

**Lamei Zhang** (Senior Member, IEEE) received the B.S., M.Sc., and Ph.D. degrees in information and communication engineering from Harbin Institute of Technology, Harbin, China, in 2004, 2006, and 2010, respectively.

She is currently an Associate Professor with the Department of Information Engineering, Harbin Institute of Technology. Her research interests include the areas of remote sensing images processing, information extraction and interpretation of high-resolution synthetic aperture radar, polarimetric SAR, and polarimetric SAR interferometry.